

## HIGH-TEMPERATURE SOLID-STATE SYNTHESIS OF Mg-DOPED ZrO<sub>2</sub>: STRUCTURAL, OPTICAL AND MORPHOLOGICAL CHARACTERIZATION

ANTONELA BERAR<sup>a</sup>, MARIETA MUREȘAN-POP<sup>b</sup>,  
LUCIAN BARBU-TUDORAN<sup>c,d</sup>, RÉKA BARABÁS<sup>e,\*</sup>, LILIANA BIZO<sup>f,\*</sup>

**ABSTRACT.** 15 at% Mg-doped ZrO<sub>2</sub> ceramic material was synthesized by solid-state reaction at 1600 °C. Particle size analysis of raw materials mixture depicts the formation of a narrow particle size distribution (PSD) with a mean particle size of about 56 nm. The structural analysis confirms that the as-synthesized Mg-doped ZrO<sub>2</sub> product is of pure tetragonal phase (*t*-ZrO<sub>2</sub>) with a crystallite size of 55.76 nm. The UV–VIS diffuse reflectance spectrum (DRS) showed a maximum %R at 550 nm and the estimated optical bandgap was about 3.83 eV. The morphology of the sample examined by scanning electron microscopy (SEM) shows interconnected grains in the sintered ceramics. Moreover, EDX analyses confirm the presence of Mg, Zr, and O, with a homogenous distribution throughout the sample.

**Keywords:** Mg-doped ZrO<sub>2</sub>, solid-state reactions, XRPD, UV-VIS spectroscopy, SEM/EDX

### INTRODUCTION

There is increasing interest in zirconia ceramics known as important candidates for functional and structural applications due to their properties which

---

<sup>a</sup> “Iuliu Hațieganu” University of Medicine and Pharmacy, Faculty of Dentistry, Department of Prosthetic Dentistry and Dental Materials, 32 Clinicilor str., RO-400006, Cluj-Napoca, Romania

<sup>b</sup> Babeș-Bolyai University, Interdisciplinary Research Institute on Bio-Nano-Sciences, 42 Treboniu Laurian str., RO-400271, Cluj-Napoca, Romania

<sup>c</sup> Babeș-Bolyai University, Faculty of Biology and Geology, Department of Molecular Biology and Biotechnology, 1 Mihail Kogălniceanu str., RO-400084, Cluj-Napoca, Romania

<sup>d</sup> National Institute for Research and Development of Isotopic and Molecular Technologies, 67-103 Donath Street, RO-400293, Cluj-Napoca, Romania

<sup>e</sup> Babeș-Bolyai University, Faculty of Chemistry and Chemical Engineering, Department of Chemistry and Chemical Engineering of Hungarian Line of Study, 11 Arany Janos str., RO-400028, Cluj-Napoca, Romania

<sup>f</sup> Babeș-Bolyai University, Faculty of Chemistry and Chemical Engineering, Department of Chemical Engineering, 11 Arany Janos str., RO-400028, Cluj-Napoca, Romania

\*Corresponding authors: breka@chem.ubbcluj.ro, lbizo@chem.ubbcluj.ro

are different and considerably improved compared with conventional ceramics. Due to its properties as excellent chemical and thermal stability, good mechanical strength, high ionic conductivity, low thermal conductivity at high temperature, high porosity and large surface area, they have been used for a wide range of industrial applications such as sensors, microelectronic devices, refractory materials, fuel cells, catalyst or catalyst support, solid-state electrolytes, thermal barrier coatings, electro-optical materials and biomaterials [1-8].

Nowadays, different types of zirconia ceramics are used for several medical applications, in replacing hard tissue due to its properties to emphasize the mechanical stability and biocompatibility [9-11]. It is widely used in medicine for replacement of the bone (hip prosthesis) but also in dentistry [12-14]. In the prosthetics domain, zirconia ceramics are used especially for fabrication of veneers, full and partial crowns, fixed partial dentures, posts and/or cores, implant abutments [15-16].

It is well known that the physical properties of  $ZrO_2$  are strongly influenced by its crystal structure. Three different forms of  $ZrO_2$  have been recognized, depending upon the growth temperature. The monoclinic phase ( $m-ZrO_2$ ) exists at low temperatures below 1150 °C and is a thermodynamically stable phase, the tetragonal phase ( $t-ZrO_2$ ) exists at intermediate temperatures within the range of 1150–2370 °C, and cubic ( $c-ZrO_2$ ) which exists at very high temperatures greater than 2370 °C [17]. The transformation from the  $t-ZrO_2$  to the  $m-ZrO_2$ , which is more stable, is associated with a volume increase of 3%-5%. Stresses generated by this expansion originate cracks in pure zirconia ceramics that, after sintering at temperatures in the range of 1500 °C -1750 °C break into pieces at room temperature. These crystal phases strongly depend on the thermal condition and preparation method [18]. To stabilize the  $t-ZrO_2$  phase at room temperature, zirconia can be mixed with other metallic oxides, e.g. CaO, MgO, CeO<sub>2</sub>, La<sub>2</sub>O<sub>3</sub>, Y<sub>2</sub>O<sub>3</sub>, etc. The addition of these oxides to pure zirconia allows to generate multiphase materials known as partially stabilized zirconia (PSZ) whose microstructure at room temperature generally consists of cubic zirconia as the major phase, with monoclinic and tetragonal zirconia precipitates as the minor phase [19-20]. The well-known system  $ZrO_2$ -Y<sub>2</sub>O<sub>3</sub> (yttria-stabilized zirconia, YSZ) has been extensively studied due to its excellent properties which make this material of special scientific and industrial interest. However, YSZ is expensive as compared with CaO- or MgO-based zirconia systems. Also, magnesia is found to be an effective dopant for stabilizing zirconia [21].

In the present paper, the facile preparation of 15 at% MgO-doped  $ZrO_2$  ceramic material by solid-state reaction at high temperature is reported. The effect of Mg doping on the structural, optical, and morphological properties, have been studied and discussed.

## RESULTS AND DISCUSSION

### Particle size analyses

Because particle size distribution (PSD) of the precursor oxide mixture is a key factor in the evolution of the solid-state reaction, laser diffraction analysis was carried out on precursor oxides,  $ZrO_2$  and MgO, and precursor oxides mixture. The PSD is presented in Figure 1.

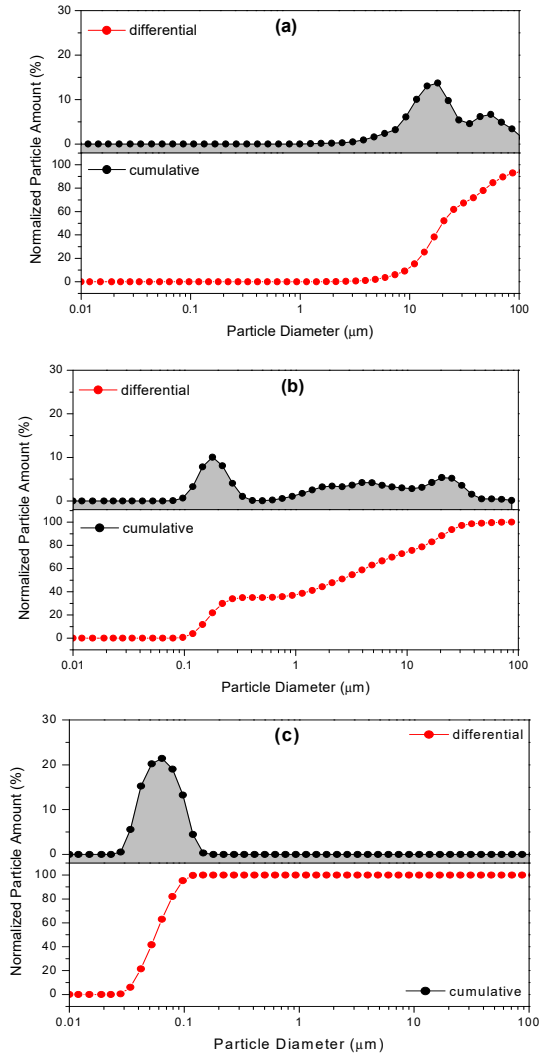


**Figure 1.** PSD (cumulative and differential curves) for (a)  $ZrO_2$ , (b) MgO and (c) raw materials mixture.

As observed from Figure 1a, for  $ZrO_2$  powder was characteristic a bimodal grain size distribution with a mean particle size of  $1,780 \mu m$  ( $SD=0.359$ ). In the case of the MgO (Figure 1b) a wide PSD of the initial  $ZrO_2$  powder, consisted of three main grain populations with a mean value of  $23.257 \mu m$  (standard deviation,  $SD=0.359$ ) was observed.

The mixture was homogenized by dry milling using an agate mortar and pestle and subsequently passed through a  $63 \mu m$  sieve. After the homogenization, the mixture consisted of a narrow PSD of particles (Figure 1c) with a mean value of  $0.056 \mu m$  ( $SD=0.146$ ). As visible from Figure 1, the volume fraction of particles smaller than  $1 \mu m$  is much higher for the mixture than for the pure  $ZrO_2$  and MgO precursor powders.

### **X-ray powder diffraction (XRPD) analysis**

To determine the structural properties of the prepared ceramic material, XRPD analysis was performed on 15 at% MgO-doped  $ZrO_2$  sintered at  $1600^\circ C$  for 12 hours. The typical XRPD patterns shown in Figure 2 provided structural information on the processed ceramic. Analysis of powder pattern of the investigated sample showed peaks at  $2\theta$  angle of  $30.5^\circ$ ,  $35.28^\circ$ ,  $50.76^\circ$ ,  $60.38^\circ$ ,  $63.36^\circ$  and  $74.7^\circ$  which correspond to the (111), (200), (220), (311), (101), and (400) crystallographic planes of *t*- $ZrO_2$  (JCPDS no. 88-1007). As evidenced from Figure 2, high peak intensity confirms the high crystallinity of the prepared material. No peaks belonging to the *m*- $ZrO_2$  or MgO phases were observed at this Mg doping level, confirming the solubility of Mg in the  $ZrO_2$ .

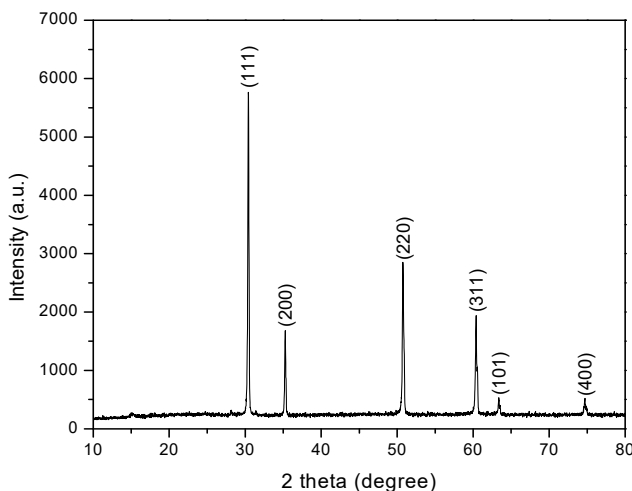


**Figure 2.** XRPD pattern of Mg-doped  $ZrO_2$ .

The small difference between ionic radii of the Zr<sup>4+</sup> (0.84 Å) and Mg<sup>2+</sup> (0.72 Å) [22] should provide the easier solubility of Mg in the ZrO<sub>2</sub> lattice, as previously observed. Consequently, the Zr<sup>4+</sup> on its lattice site is substituted by the Mg<sup>2+</sup> ion. Furthermore, since Mg has the oxidation state of +2, some oxygen vacancy is induced in the structure. It has been previously reported that oxygen vacancies are the main reason for the stabilization of the tetragonal phase [23].

The crystallite size (D) of the prepared composition was calculated by Scherrer formula for (111) reflection:

$$D_{hkl}=0.9\lambda/(\beta\cos\theta) \quad (1)$$

where: D - crystallite size along (hkl) direction,  $\beta$  - full width half maximum (FWHM) of the most intense diffraction line,  $\lambda$  - wavelength of X-ray,  $\theta$  - the Bragg angle [24].

The calculated crystallite size of Mg-doped ZrO<sub>2</sub> was about of 55.67 nm. Compared with data obtained by laser diffraction it can be stated that the size of particles remains practically unchanged after sintering. This phenomenon was previously observed on the sintering of nanostructured ZrO<sub>2</sub> ceramics by colloidal processing. The inhibition of the grain growth may have been caused by inter-diffusion of cations during the sintering [25].

### **UV-VIS spectroscopy**

The optical properties of the prepared composition were considered in terms of UV-VIS diffuse reflectance spectrum (DRS) as shown in Figure 3a. The DRS spectrum shows a sharp and prominent maximum %R around 550 nm which can arise due to the transition between valence band to the conduction band.

Figure 3b revealed the optical bandgap (E<sub>g</sub>) value estimated from DRS by Tauc plot using Kubelka-Munk function F(R) [26]. The determination of E<sub>g</sub> by applying the Kubelka–Munk (K–M or F(R)) method is based on the following equation:

$$F(R) = (1-R)^2/2R \quad (2)$$

where R is the reflectance; F(R) is proportional to the extinction coefficient ( $\alpha$ ).

The bandgap of ZrO<sub>2</sub> is dependent on heat treatment temperature as shown by Lavisa et al. [27]. Their result indicates that the exponential optical absorption edge and optical bandgap are controlled by the degree of structural defects in the lattice. Hence, the increase of optical bandgap value with the heat treatment temperature promotes a reduction of the intermediary energy levels, as a result of the structural organization in the lattice [27, 28]. The bandgap can be also influenced by the formation methods and type and

amount of dopant introduced in the  $\text{ZrO}_2$  lattice. Depending on the types and chemical states of metal ions, the bandgaps of metal-doped  $\text{ZrO}_2$  varied, the differences being mainly associated with the electronic configurations of the ions, which control the energy levels in the  $\text{ZrO}_2$ .

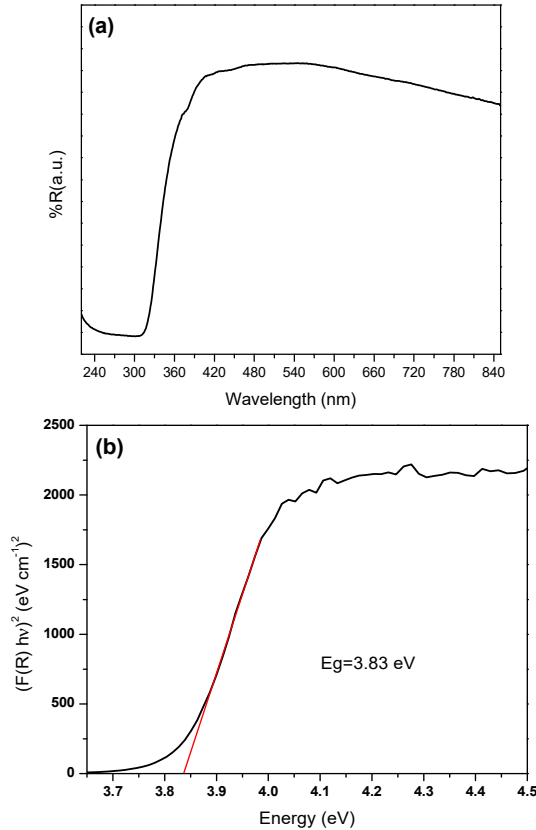


**Figure 3.** (a) DRS of Mg-doped  $\text{ZrO}_2$  and (b) the Tauc plot depicting the optical bandgap.

In our work, the bandgap determined for the bulk Mg-doped  $\text{ZrO}_2$  ceramic material from the DRS spectrum is about 3.83 eV.  $\text{ZrO}_2$  has a wide bandgap, and the reported value is about 5.0 eV [29]. The reduced value of bandgap obtained for Mg-doped  $\text{ZrO}_2$  may be due to the incorporation of magnesia. In the case of Mg doping in  $\text{ZrO}_2$ ,  $\text{Mg}^{2+}$  ions are moved to the substituted sites in the  $\text{ZrO}_2$  matrix and may act as a donor impurity. The doped  $\text{Mg}^{2+}$  ions increase the donor density and thus result in the formation of a donor level below the conduction band thereby reducing the bandgap of  $\text{ZrO}_2$  [30].

### Scanning electron microscopy (SEM) / Energy dispersive X-ray (EDX) spectroscopy

SEM was employed to analyze the morphological characteristics of the prepared Mg-doped  $ZrO_2$  ceramic material. From the images shown in Figure 4(a, b, c), it can be seen that irregular and agglomerated shapes like morphology was formed in the ceramic sample.

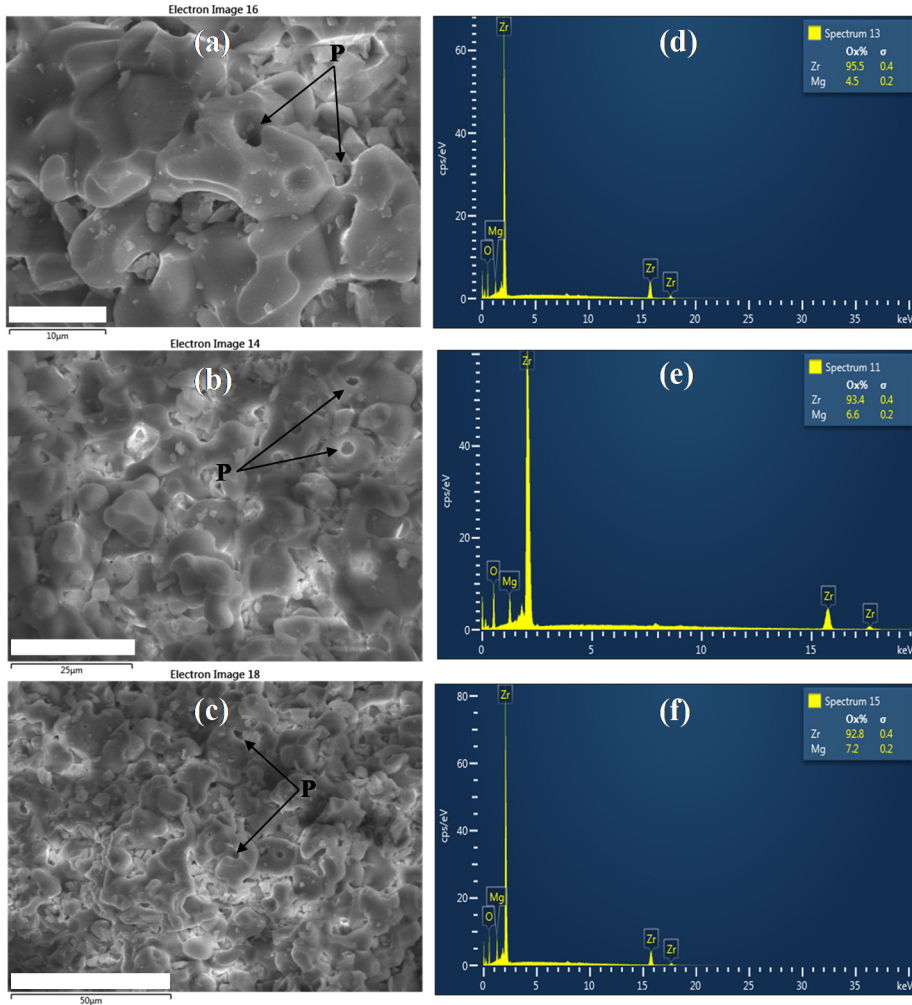


**Figure 4.** SEM images at different magnifications (a, b and c) and typical corresponding EDX spectra (d, e and f) of Mg-doped  $ZrO_2$  ceramics. The corresponding scale bars are (a) 10  $\mu m$ , (b) 25  $\mu m$  and (c) 50  $\mu m$ , respectively.

SEM data reveals also that the grains are stronger interconnected to each other. This typical interconnected structure in zirconia-based ceramics was previously observed for yttria-stabilized zirconia (YSZ) ceramics or  $ZrO_2$ -based composites, sintered at  $1550\text{ }^\circ\text{C}$  [31, 32]. As stated before, this strong network provided by the interconnection of grains allows to obtain high mechanical strength [31]. In addition, the microstructural observations reveal the presence of pores as seen in Figure 4. From point of view of technological applications one of the most important characteristics of the porous YSZ is low thermal conductivity, which is greatly influenced by the presence of pores into the microstructure. The air trapped in the pores represents a better thermal insulator [33]. For biomedical applications finer pores and less volume fraction of porosity should be beneficial for biological cell attachment. The presence of finer pores could favor the initial osteoblast cell attachment by a mechanical anchorage process. Consequently, once cells are attached at the initial stage of implantation, the attached cell assembly would subsequently favor formation of multiple cells and thereby lead to *in vivo* tissue formation [34, 35].

The chemical composition of the obtained Mg-doped  $ZrO_2$  ceramic material was analyzed using EDX as displayed in Figure 4(d, e, f). The EDX result confirms the presence of elements such as magnesium, oxygen and zirconium by the appearance of Mg, Zr and O peaks. It indicates the purity of the product and without any other signal present in the product.

Qualitative analysis of elements present in Mg-doped  $ZrO_2$  ceramic sample was further evaluated by elemental mapping. The elemental mapping micrographs are presented in Figure 5.

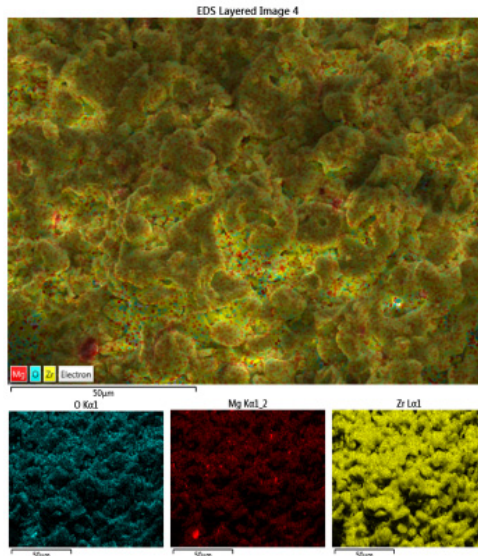


**Figure 5.** SEM mapping photographs for the Mg-doped  $ZrO_2$  ceramic.

These micrographs confirmed the homogenous distribution of the elements in the sample. It was found that magnesia is distributed uniformly throughout the imaged area, which clearly indicates that the ZrO<sub>2</sub> is surface modified by magnesia.

## CONCLUSIONS

15 at% Mg-doped ZrO<sub>2</sub> ceramic material was successfully obtained by solid-state reaction method at 1600°C, followed by their characterization using XRPD, UV-VIS, and SEM techniques. The analyses indicated the presence of *t*-ZrO<sub>2</sub> phase. No trace of the *m*-ZrO<sub>2</sub> or MgO phase was noticed in the sample. The SEM micrographs confirmed the homogenous distribution of the elements through the mixed oxide. Further, optical properties evaluated in terms of UV-VIS DRS spectrum, revealed that the Mg-doped ZrO<sub>2</sub> showed a smaller bandgap compared with pure ZrO<sub>2</sub>, which may be due to the incorporation of magnesia in the ZrO<sub>2</sub> matrix. Moreover, through this study, we have confirmed the significant role played by the Mg<sup>2+</sup> aliovalent dopant cation concerning *t*-ZrO<sub>2</sub> phase stabilization. The study also should be helpful in the development of potential applications using Mg-doped ZrO<sub>2</sub>, like catalysis, sensors, energy conversion and storage, coating, or in the biomedical domain.

## EXPERIMENTAL SECTION

### PREPARATION

#### *Ceramic preparation*

Mg-doped ZrO<sub>2</sub> ceramic sample was synthesized by solid-state reaction at high temperature following the scheme from Figure 6.

Commercial pure ZrO<sub>2</sub> (Riedel-de Haën AG, Seelze, Germany, 99%) and MgO (Alfa Aesar, Germany, 99.99%) powdered oxides were used as starting materials in order to obtain 15 at% MgO in ZrO<sub>2</sub>. Proper amounts of starting precursors in a corresponding atomic ratio were homogenized using an agate mortar and pestle. The resultant powder was mixed with 5% PVA and uniaxially cold-pressed in a metallic die into cylindrical pellets of 1 g with 10 mm in diameter at a pressure of 400 kgf/cm<sup>2</sup> using a Carver Inc. hydraulic press (Carver Inc, Wabash, IN, USA). The obtained pellets were further sintered at 1600 °C under the air atmosphere using a high-temperature Nabertherm LHT 04/16 furnace, with a heating and cooling rate of 5 °C/min and dwell time of 12 h at the maximum temperature.

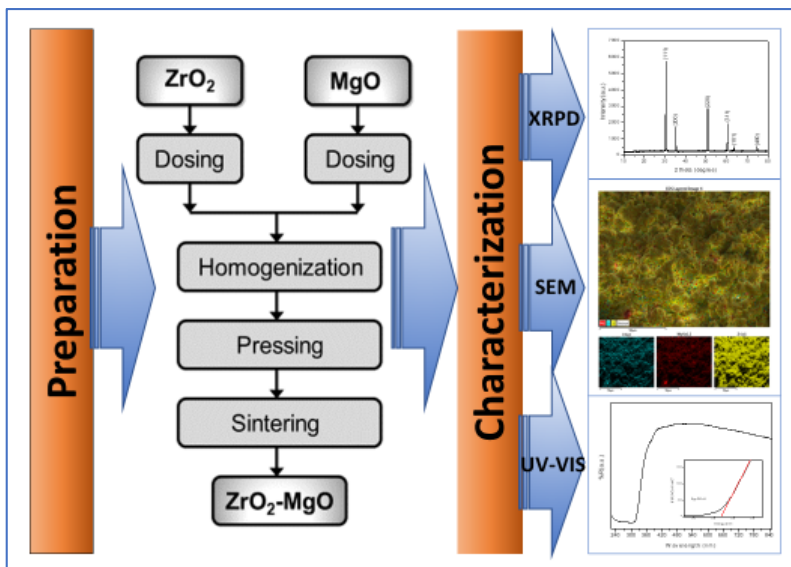


Figure 6. Schematic flowchart for Mg-doped ZrO<sub>2</sub> ceramic preparation.

## CHARACTERIZATION METHODS

### *Particle size analysis*

A Shimadzu Sald-7101 (Japan) micro- and nano- particle size analyser was used for investigating the particle size distribution (PSD) of raw materials and raw materials mixture powders. Samples were immersed for 15 s in distilled water used as a solvent, with aggregation being reduced using treatment with ultrasounds.

### *X-ray powder diffraction (XRPD)*

XRPD analysis was performed in order to investigate the structure of the samples, using a Shimadzu XRD-6000 (Japan) diffractometer operating at 40 kV, 30 mA with a monochromator of graphite for CuK $\alpha$  ( $\lambda=1.5418$  Å). The diffraction patterns was recorded in the  $2\theta$  range of 10–80° at a scan speed of 2 °/min.

### *Scanning Electron Microscopy (SEM)/ Energy dispersive X-ray (EDX) spectroscopy*

SEM analysis was performed using a Hitachi SU8230 (Tokyo, Japan) microscope. The electron microscope was coupled with an Aztec X-Max 1160 EDX detector (Oxford Instruments).

### **UV-VIS spectroscopy**

UV-VIS spectroscopy was employed to characterize the influence of the dopant on the optical properties of the ZrO<sub>2</sub> based ceramic. Diffuse reflectance spectrum (DRS) was registered with a double-beam JASCO V-650 (Japan) spectrophotometer, equipped with an ISV-722 Integrating Sphere, in the wavelength range from 200 to 800 nm, with a scan rate of 400 nm/min.

### **ACKNOWLEDGEMENTS**

This work is a contribution to the COST (European Cooperation on Science and Technology) Action CA18112- Mechanochemistry for Sustainable Industry (M. M.-P. and L. B.).

### **REFERENCES**

1. S. Shukla; S. Seal; *Int. Mater. Rev.*, **2005**, 5, 45–64.
2. D.R. Clarke; C.G. Levi; *Annu. Rev. Mater. Res.*, **2003**, 33, 383–417.
3. J.Y. Thompson; B.R. Stoner; J.R. Piascik; R. Smith; *Dental Mater.*, **2011**, 27, 71–82.
4. V. Fiorentini; G. Gulleri; *Phys. Rev. Lett.*, **2002**, 89, 266101, 1–4.
5. P. Li; I. W. Chen; J.E. Penner-Han; *J. Am. Ceram. Soc.*, **1994**, 77, 118–128.
6. D. Ysoutsou; G. Apostolopoulos; S. Galata; A. Sotiropoulos; G. Mavrou; Y. Panayiotatos; A. Dimoulas; *Microelect. Eng.*, **2009**, 86, 1626–1628.
7. S. Manjunatha; M.S. Dharmaprasath; *J. Luminescence*, **2016**, 180, 20–24.
8. S. Somiya; N. Yamamoto; H. Yanagita; *Science and Technology of Zirconia (III)*, vol. 24 A and 24B, American Ceramic Society, Westerville, **1988**.
9. S. Raveendrana; M.I.K. Khanb; A. Dhayanb; S. Kannan; *Ceram. Int.*, **2020**, 46, 641–652.
10. P.F. Manicone; P. Rossi Iommetti; L. Raffaelli; *J. Dent.*, **2007**, 35, 819–826.
11. I.G. Tredici; M. Sebastiani; F. Massimi; E. Bemporad; A. Resmini; G. Merlati; U. Anselmi-Tamburini; *Ceram. Int.*, **2016**, 42, 8190–8197.
12. S. Kargozar; S Ramakrishna; M. Mozafari. *Curr. Opin. Biomed. Eng.*, **2019**, 10, 181–190.
13. S. Soon; B. Pingguan-Murphy, K.W Lai; S.A. Akbar; *Ceram. Int.*, **2016**, 42(11), 12543–12555.
14. O.S. El-Ghany; A.H Sherief; *Future Dent. J.*, **2016**, 2(2), 55–64.
15. S.A. Ali; S. Karthigeyan; M. Deivanai; R. Mani; *Pak. Oral Dent. J.*, **2014**, 34, 177–183.

16. M. Ferrari; A. Vichi; F. Zarone; *Dent. Mater.*, **2015**, 31(3), e63–e76.
17. S. Kumar, S. Bhunia, A.K. Ojha, *Chem. Phys. Lett.*, **2016**, 644, 271–275.
18. L. Renuka, K.S. Anantharaju, S.C. Sharma, H.P. Nagaswarupa, S.C. Prashantha, H. Nagabhushana, Y.S. Vidya, *J. Alloys Compd.*, **2016**, 672, 609-622.
19. E.C. Subbarao. Zirconia-an overview. In: *Advances in ceramics*, A.H. Heuer, L.W. Hobbs, Science and Technology of Zirconia, Amsterdam: Elsevier, **1981**, vol 3, 1-24.
20. C. Piconi; G. Maccauro; *Biomaterials*, **1999**, 20, 1-25.
21. L. Keerthana; C. Sakthivel; I. Prabha; **2019**, 3-4, *Materials Today Sustainability*, 100007, 1-15.
22. R.D. Shannon; C.T. Prewitt; *Acta Cryst.*, **1969**, B25, 925-946.
23. S. Shukla; S. Seal; **2005**, *Int. Mater. Rev.* 50(1), 45-64.
24. A.L. Patterson; *Phys. Rev.*, **1939**, 56, 978-982.
25. G. Suárez; Y. Sakka; T. S Suzuki; T. Uchikoshi; X. Zhu; E.F. Aglietti; *Sci. Technol. Adv. Mater.*, **2009**, 10(2), 025004, 1-8.
26. P. Kubelka; F. Munk-Aussig; *Physik*, **1931**, 12, 593-601.
27. L.X. Lovisa; V.D. Araújo; R.L. Tranquilin; E. Longo; M.S. Li; C.A. Paskocimas; M.R.D. Bomio; F.V. Motta; *J. Alloys Compds.*, **2016**, 674, 245-251.
28. M.D. Gonçalves; L.S. Cavalcante; J.C. Sczancoski; J.W.M. Espinosa; P.S. Pizani; E. Longo; I.L.V. Rosa; *Opt. Mater.*, **2009**, 31, 1134-1143.
29. A. Emeline; G.V. Kataeva; A.S. Litke; A.V. Rudakova; V.K. Ryabchuk; N. Serpone, *Langmuir*, **1998**, 14, 5011-5022.
30. Y. Nian-Qi; L. Zhi-Chao; G. Guang-Rui; W. Bao-Jia; *Chinese Physics B*, **2017**, 26(10), 106801, 1-5.
31. L. Hu; C. Wang; Y. Huang; *J. Mater. Sci*, **2010**, 45, 3242–3246.
32. L. Bizo; K. Sabo; R. Barabas; G. Katona; L. Barbu-Tudoran; A. Berar; *Studia UBB Chemia*, LXV, 1, **2020**, 137-148.
33. G. Pia; C. Siligardi; L. Casnedi; U. Sanna, *Ceram. Int.*, **2016**, 42(8), 9583-9590.
34. B. Annaz; K.A. Hing; M. Kayser; T. Buckland; L. Di Silvio; *J. Microsc.*, **2004**, 215, 100-110.
35. S. Nath; S. Baja; B. Basu; *Int. J. Appl. Ceram. Technol.*, **2008**, 5(1), 49-62.